

Article

Transmission Electron Microscopy of a CMSX-4 Ni-Base Superalloy Produced by Selective Electron Beam Melting

Alireza B. Parsa ^{1,*}, Markus Ramsperger ², Aleksander Kostka ¹, Christoph Somsen ¹, Carolin Körner ² and Gunther Eggeler ¹

¹ Institut für Werkstoffe, Ruhr-Universität Bochum, Universitätsstr. 150, Bochum 44801, Germany; aleksander.kostka@rub.de (A.K.); christoph.somsen@rub.de (C.S.); gunther.eggeler@rub.de (G.E.)

² Lehrstuhl WTM, Friedrich-Alexander-Universität Erlangen-Nürnberg, Martensstr. 5, Erlangen 91058, Germany; markus.ramsperger@fau.de (M.R.); carolin.koerner@ww.uni-erlangen.de (C.K.)

* Correspondence: alireza.basirparsa@rub.de; Tel.: +49-234-32-27898

Academic Editor: Jonathan Cormier

Received: 12 September 2016; Accepted: 21 October 2016; Published: 28 October 2016

Abstract: In this work, the microstructures of superalloy specimens produced using selective electron beam melting additive manufacturing were characterized. The materials were produced using a CMSX-4 powder. Two selective electron beam melting processing strategies, which result in higher and lower effective cooling rates, are described. Orientation imaging microscopy, scanning transmission electron microscopy and conventional high resolution transmission electron microscopy are used to investigate the microstructures. Our results suggest that selective electron beam melting processing results in near equilibrium microstructures, as far as γ' volume fractions, the formation of small amounts of TCP phases and the partitioning behavior of the alloy elements are concerned. As expected, higher cooling rates result in smaller dendrite spacings, which are two orders of magnitude smaller than observed during conventional single crystal casting. During processing, columnar grains grow in $\langle 100 \rangle$ directions, which are rotated with respect to each other. There are coarse γ/γ' microstructures in high angle boundary regions. Dislocation networks form low angle boundaries. A striking feature of the as processed selective electron beam melting specimens is their high dislocation density. From a fundamental point of view, this opens new possibilities for the investigation of elementary dislocation processes which accompany solidification.

Keywords: Ni-base superalloy; selective electron beam melting; evolution of microstructure; transmission electron microscopy; ingrown dislocations

1. Introduction

Ni-base single crystal superalloys are cast materials, which are used to make blades for gas turbines in aero engines and power plants [1–3]. In the last decades, directionally solidified (DS) and single crystal superalloys (SX) and their processing techniques were continuously improved and this led to the high performance of today's gas turbines. Turbine blades operate in the creep range where they have to withstand mechanical loads in the 1000 °C temperature range. In the present work, the superalloy CMSX-4 is considered. This second generation superalloy contains refractory alloy elements like W, Ta, and Re. These elements provide good creep strength because their atomic mobility is low, which retards dislocation climb in the γ and in the γ' phase [4]. It is well known and it has been recently shown for the single crystal superalloy ERBO-1 (CMSX-4 derivative) [5] that cast Ni-base superalloys are prone to segregation during solidification. There are distinct differences between former dendrites and interdendritic regions. As a result, cast SX are characterized by a microstructural and chemical heterogeneity on the length scale of the dendrite spacing (average value: 500 μm [5]).

The complex multiple step homogenization heat treatments which are used in industry do not fully re-establish microstructural and chemical homogeneity [4,5]. Another matter of concern in this context is the formation of cast micro pores during solidification of single crystal superalloys [6,7]. These form between secondary dendrite arms and line up along primary dendrites [6,7]. They can represent initiation sites for creep and fatigue cracks [6,8]. Both, chemical/microstructural heterogeneity and cast porosity can be reduced by refining the microstructure. It was realized early on that high solidification rates are desirable in order to refine microstructures and improve mechanical properties. This has led to the development of techniques like liquid metal cooling [9] and continuing efforts in this direction to further improve SX cast technology. However, industrial efforts in the cast sector will always represent a compromise between homogeneity/micro pore presence and cost effectiveness, i.e., the duration of homogenization times at elevated temperatures will always be limited.

A process which does not suffer from this drawback is selective electron beam melting (SEBM) [4,10–14], which can produce complex shapes [10]. SEBM is characterized by a layered build architecture offering novel possibilities for component design [4,10–14]. SEBM represents a powder bed additive manufacturing technology which has a high potential to process superalloys in the future. SEBM is characterized by high solidification rates and high thermal gradients. Therefore, the scale of segregation and the primary dendrite arm spacings can be two orders of magnitude smaller as compared to cast SX. This refinement of critical microstructural features represents an advantage of SEBM for superalloy processing. The topic is presently receiving attention in the literature, e.g., [4,12]. So far, microstructural characterization of SEBM fabricated Ni-base superalloys was mainly performed using scanning electron microscopy (SEM) [4,10–14] and results obtained by transmission electron microscopy are scarce [12]. The present work builds on earlier work [4,13,14] and use orientation imaging microscopy (OIM) and transmission electron microscopy (TEM) to study the microstructures of two SEBM material states, which were produced applying two sets of processing parameters which promote a coarser and a finer microstructure, respectively. The objective of the present work is to identify these differences and to discuss the results in the light of previous work reported in the literature.

2. Materials and Methods

2.1. Material

In this study, microstructures produced by SEBM are assessed. The SEBM processing route requires powders, which are obtained by gas atomizing of CMSX-4 [4]. CMSX-4 bar stocks were provided by Cannon Muskegon. The material was atomized with Argon using an electrode induction-melting gas atomization (EIGA) process by TLS Technik Spezialpulver KG (Bitterfeld, Germany). The CMSX-4 powder had a bulk density of 56%, and a flow time of $21.3 \text{ s} \pm 0.3 \text{ s}$ (50 g powder) through a 2.54 mm notch was determined. Powder particle sizes range between 45 μm and 105 μm . The chemical composition of the powder was measured using induction coupled plasma atomic emission spectroscopy. The composition is presented in Table 1.

Table 1. Chemical composition of CMSX 4 powder (induction coupled plasma atomic emission spectroscopy data) in wt. %.

Element	Al	Co	Cr	Hf	Mo	Re	Ta	Ti	W	Ni
Composition	5.70	9.80	6.50	0.08	0.62	2.80	6.40	0.97	6.40	bal.

2.2. SEBM Processing

Two bulk samples (sample A: $15 \times 15 \times 10 \text{ mm}^3$; sample B: $5 \times 5 \times 20 \text{ mm}^3$) were investigated in the present study. They were fabricated in an ARCAM A2 electron beam melting system. The process is schematically illustrated in Figure 1. The system operates at 60 kV accelerating voltage in a 10^{-3} mbar

helium atmosphere. The SEBM specimens were build up in 50 μm layers on an IN 718 starter plate kept at the build temperature $T_B = 1150$ K. The SEBM processing parameters for the two different processing strategies are listed in Table 2. As illustrated in Figure 1a, first a 50 μm powder layer is deposited. The powder is subsequently preheated by a scanning procedure with a strongly defocused electron beam to an appropriate temperature. During the following melting step, the focused electron beam (beam diameter approximately 400 μm) scans across the specimen surface and consolidates the powder particles to denser material. Finally, the working level is lowered by 50 μm , before the next powder layer is deposited. This process is repeated until the sample has reached its targeted dimensions.

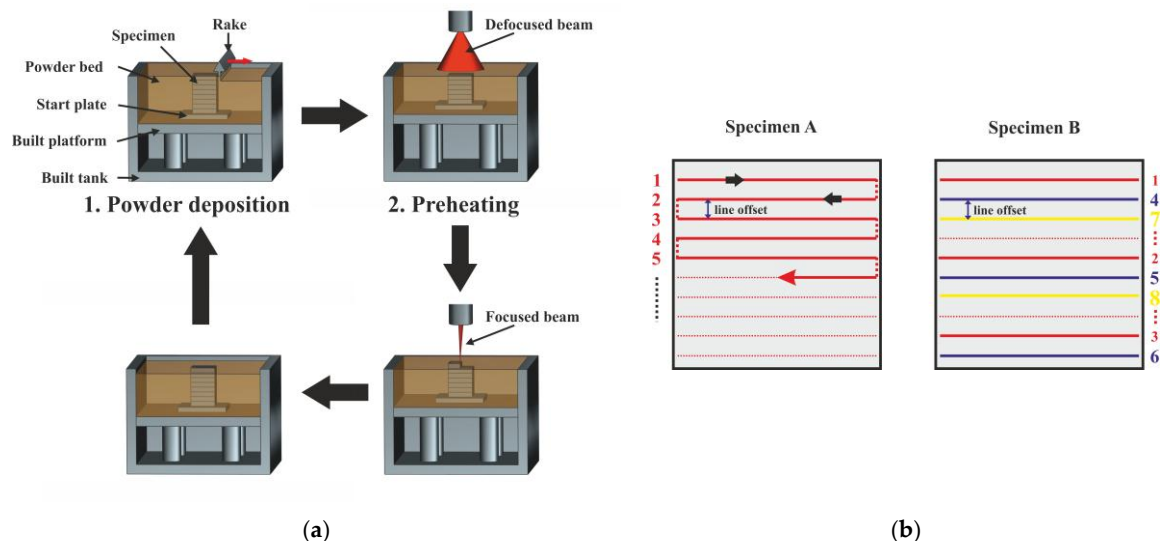


Figure 1. Schematic illustration of SEBM procedure: (a) SEBM processing steps; and (b) two types of scan strategies referred to as line order 1 (Specimen A) and 5 (Specimen B), and their subsequent processing steps.

Table 2. Parameters used for SEBM processing of Specimens A and B.

Specimen	Volume/ mm^3	T_B/K	Power/W	Scan Speed/(mm/s)	Line Offset/ mm	Line Order/-
A	2250	1150	480	2400	0.1	1
B	500	1150	300	500	0.1	5

Two different beam scan strategies were applied for Specimens A and B, as schematically illustrated in Figure 1b. In the case of sample A, the beam scans 15 mm in the forward direction, then, with 0.1 mm line offset, it moves 15 mm back. Then, after another 0.1 mm line offset it moves forward again. In SEBM technology, this type of beam movement is referred to as hatching. The beam moves in a snake-like back and forth manner. When the electron beam has scanned over the whole specimen surface, one powder layer has been molten and solidified. In the next layers, the hatching direction is rotated by 90°. This also applies to the SEBM procedure of Specimen B. However, in the case of Specimen B, electron beam scanning is controlled in a different manner. The distance between the first and the second line (shown in red and numbered 1 and 2 in Figure 1b) is now 0.5 mm. The third line (red line numbered 3) is 0.5 mm distance from line 2. In our schematic figure, the bottom of the specimen is reached after the third step (in the real SEBM processing of Specimen B, 10 steps are required). The next series of electron beam scan lines (blue lines 4 to 6) follows exactly the same pattern as the first series (red lines 1 to 3), however it is offset by 0.1 mm. Five such series are required to establish the same line offset of 0.1 mm as in the process used for Specimen A. In the field of additive

manufacturing, these two procedures are referred to as line order 1 (Specimen A) and line order 5 (Specimen B).

Figure 2a,b shows photographs of Specimens A and B, respectively. Both specimens have rough surfaces since contour melting was not applied. The SEBM build directions (BD) are indicated by arrows.

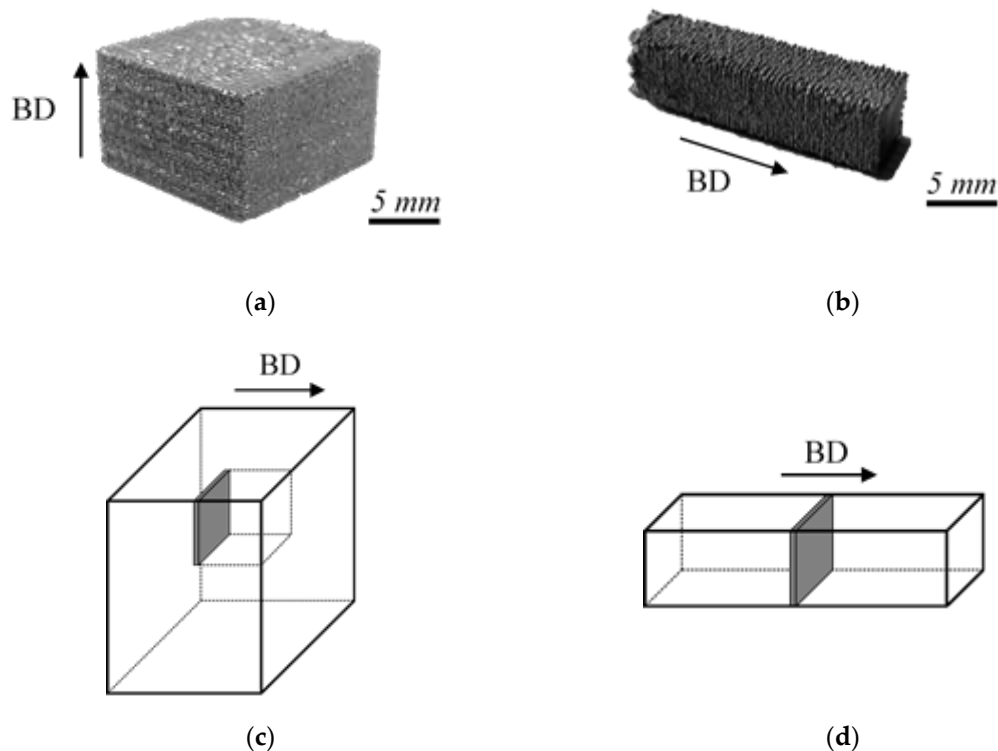


Figure 2. SEBM specimens investigated in the present work, where the arrows indicate the build direction (BD) of the SEBM blocks: (a) Specimen A; and (b) Specimen B. (c,d) Schematic illustration of locations where samples for microstructural characterization were taken out: (c) sample taken out from Specimen A; and (d) sample taken out from Specimen B.

2.3. Microstructural Characterization

Figure 2c,d schematically illustrates where cross sections for microstructural investigation were taken out from the two SEBM Specimens A and B. After the TEM specimens were cut out using an Accutom 50 precision cutting machine, thin electron transparent foils were prepared by grinding (down to a mesh size of $4\ \mu\text{m}$) followed by double jet electropolishing in a Struers TenuPol 5 (Ballerup, Denmark). Good thinning conditions were obtained using an electrolyte consisting of 75% methanol, 15% perchloric acid and 10% glycerol at 12 V, $-5\ ^\circ\text{C}$ and a flow rate of 35 a.u. These thin foils were used for TEM and subsequent SEM investigations. From the electropolished thin foil, regions of constant thickness were cut out for local chemical analysis using a focused ion beam (FIB) system. Ion milling was performed using a dual beam FIB of type Quanta 200 3D from FEI (Hillsboro, OR, USA). A TEM of type Tecnai Supertwin F20 (FEI, Hillsboro, OR, USA) equipped with an X-ray energy dispersive spectrometer (EDS) and a high angle annular dark field (HAADF) detector operating at 200 kV was used. All scanning transmission electron microscope (STEM) images were acquired in nano-probe mode except images in Figure 6a,c, which were taken in micro-probe mode. SEM investigations were performed using two SEMs, one of type FEI Quanta 650 (operating at 20 kV) and another of type JEOL JSM-6490 (also operating at 20 kV). The Quanta 650 machine was used for taking overview images. The JSM-6490 was used for electron backscatter diffraction analysis. If not stated otherwise, microstructural images shown in this study represent cross sections which were taken perpendicular

to the SEBM build direction (solidification direction). Scanning transmission electron microscopy (STEM) and stereo STEM were performed as described in [15]. The stereo STEM method was used to provide anaglyphs, which show the microstructures of high and low angle boundaries. A simple line intersection method was used to tentatively determine γ' sizes and volume fractions from STEM images. Tentative values for dendrite spacings were obtained based on counting the numbers of dendrites in projected TEM foil areas.

From the processing condition listed in and the image cut up plans shown in Figure 2, it is clear that different types of material are compared (different scan strategies and thus different cooling rates, and different TEM foil positions). However, it is clear that the material in the TEM foil which was taken from the surface region of Specimen A has experienced a faster cooling rate than the material of the TEM foil which was taken from Specimen B. In the present work, TEM is used to compare two material states resulting from slow (Specimen B) and fast cooling (Specimen A).

3. Results

3.1. Grain Size and Grain Orientation

In Figure 3, SEM micrographs are presented which were taken using electron back scatter contrast. The SEM images shown in Figure 3a,b clearly prove that SEBM Specimen A (fast cooling) has a finer microstructure than Specimen B (slower cooling). Figure 3 also suggests that smaller groups of dendrites form with specific orientations which differ from each other (light and dark grey contrasts). This is confirmed in the electron backscattered diffraction (EBSD) images presented in Figure 4. Figure 4a,d shows inverse pole figures (IPF maps) for both SEBM pieces, which provide color coded orientation information. The color code indicates that red represents a $\langle 001 \rangle$ direction. It can be clearly seen that the predominant color in Figure 4a,d is red. This allows us to conclude that the SEBM growth direction of individual grains is close to $\langle 100 \rangle$, independent of the line scan strategy and independent of the geometry of the manufactured piece. Figure 4b,e show image quality maps (IQ maps). These images show dark local contrast where crystal defects are present and indicate the presence of internal boundaries. The IQ maps in Figure 4b,e (calculated from the same data which are used to obtain the IPF maps in Figure 4a,d) also clearly indicate the presence of internal boundaries. They are helpful in the present case, where all grains appear in a similar red color in the IPF maps. Figure 4c,f shows EBSD results, which combine IPF- and IQ-information.

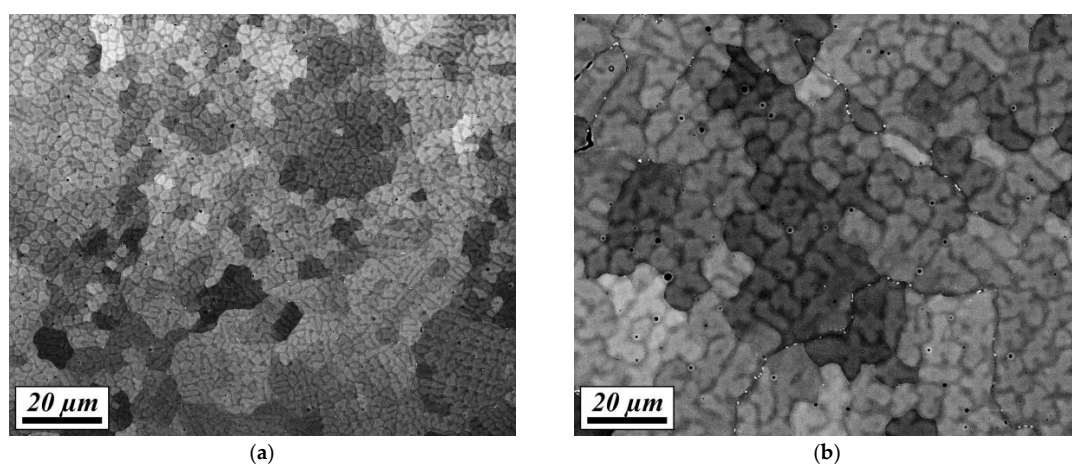


Figure 3. SEM-BSE images: (a) SEBM Specimen A; and (b) SEBM Specimen B.

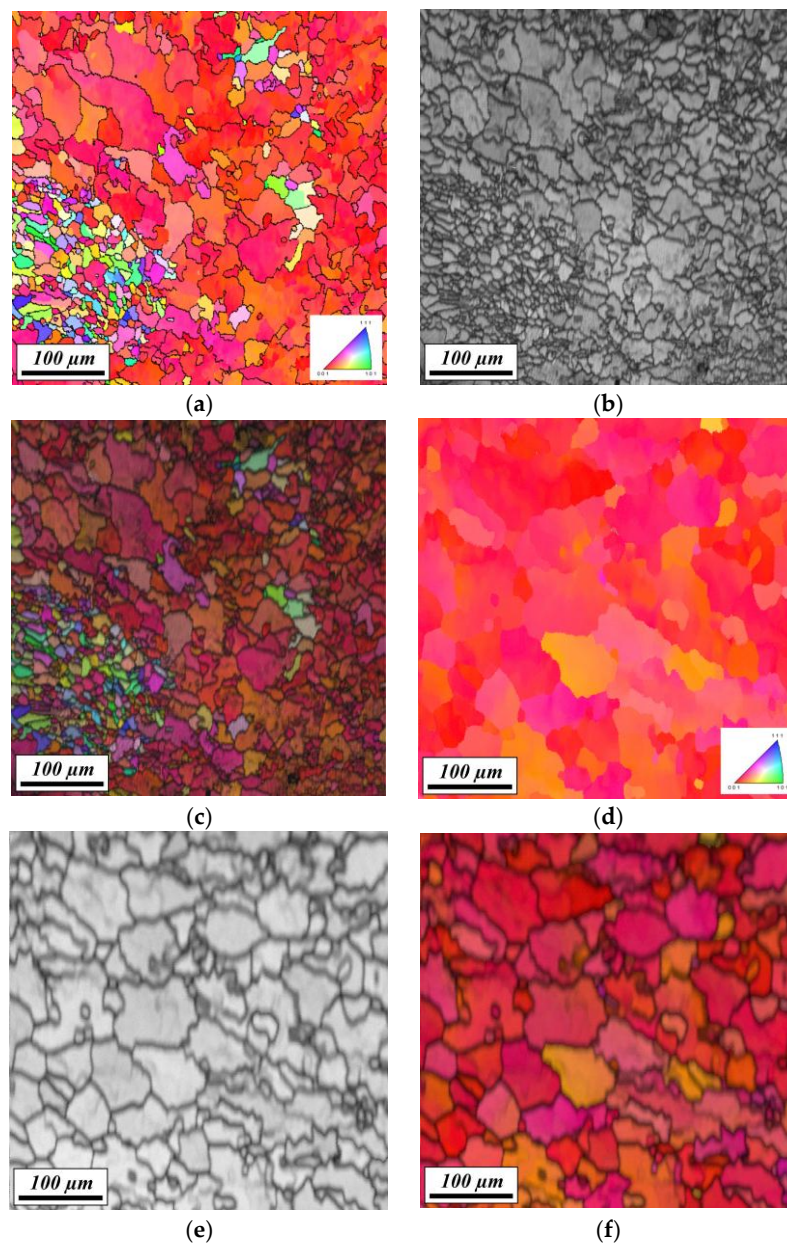


Figure 4. EBSD results: (a–c) SEBM Specimen A; (d–f) SEBM Specimen B; (a,d) IPF-maps; (b,e) IQ-maps; and (c,f) combined IPF/IQ-maps.

EBSD data can be analyzed to determine tilt axis/tilt angle pairs, which can be used to describe the misorientation between two crystallites (Figure 5) [16,17]. Figure 5 shows images where grain boundary misorientations are superimposed onto the IQ maps shown in Figure 4b,e. In Figure 5, one can differentiate between three color coded angular groups. Misorientations smaller than 2° are not highlighted. Low angle misorientations between 2° and 5° are marked in red. Green lines indicate misorientations between 5° and 15° . Misorientations larger than 15° are shown in blue.

Figure 5 clearly shows that, in both microstructures, a considerable part of the columnar grains show misorientations which are larger than 2° and therefore do not qualify as low angle grain boundaries.

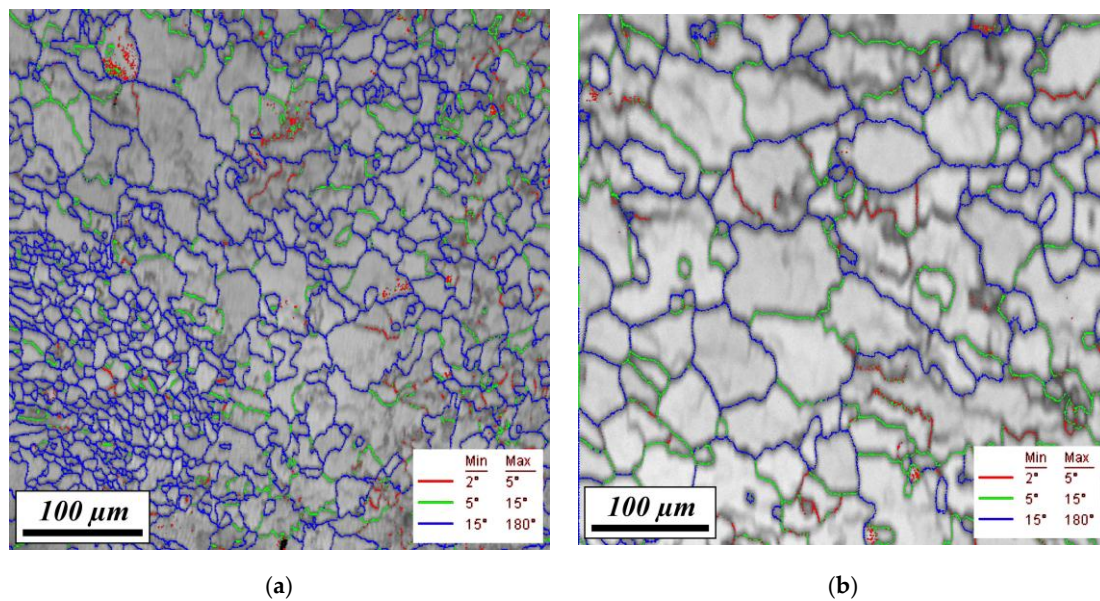


Figure 5. Misorientations between adjacent grains. Three misorientation classes are highlighted as indicated. Grain boundaries with misorientations smaller than 2° are not highlighted: (a) SEBM Specimen A; and (b) SEBM Specimen B.

3.2. TEM Results

In Figure 6, TEM images are presented which were obtained for the two material states (SEBM Specimen A: Figure 6a,b; SEBM Specimen B: Figure 6c,d) using multiple beam contrast in the STEM-HAADF mode. Figure 6a,c was taken at lower magnifications (STEM micro-probe mode). Figure 6b,d represents the microstructures at higher magnifications. Note that the magnification of Figure 6a (Specimen A) is higher than that for Specimen B in Figure 6c. The TEM results confirm the SEM findings reported above. The microstructure of Specimen A is much finer than that of Specimen B. A comparison between Figure 6a (SEBM Specimen A), 6c (SEBM Specimen B) reveals additional distinct differences. In Specimen A, no secondary dendrite arms can be distinguished. In contrast, Specimen B shows the typical cross like appearance, which characterizes dendrites cut perpendicular to their growth direction (one highlighted with a white arrow). The micrographs presented in Figure 6b,d reveals that there are in both specimens small bright particles. Later, it is shown that these are μ phase particles, which are known to have a rhombohedral crystal structure (space group: $R\bar{m}\bar{3}$). They appear at the boundaries that separate regions of homogeneous crystallographic orientation (two highlighted by small horizontal white arrows for each material state). Their volume fractions are always small, but they are larger in Specimen B than in Specimen A. Moreover, in Specimen B, one finds large γ' regions (two highlighted by a vertical arrow in Figure 6d). These regions were identified by diffraction as γ' (not shown here). The magnifications the micrographs presented in Figure 6 was chosen so in order to show similar number of dendrites (Figure 6a,c) and to show the presence of μ phase between regions of heterogeneous crystallographic orientations (Figure 6b,d). Specimen B shows a lower dislocation density; in fact, it is difficult to distinguish dislocations in Figure 6d. Figure 6d is shown to demonstrate columnar regions.

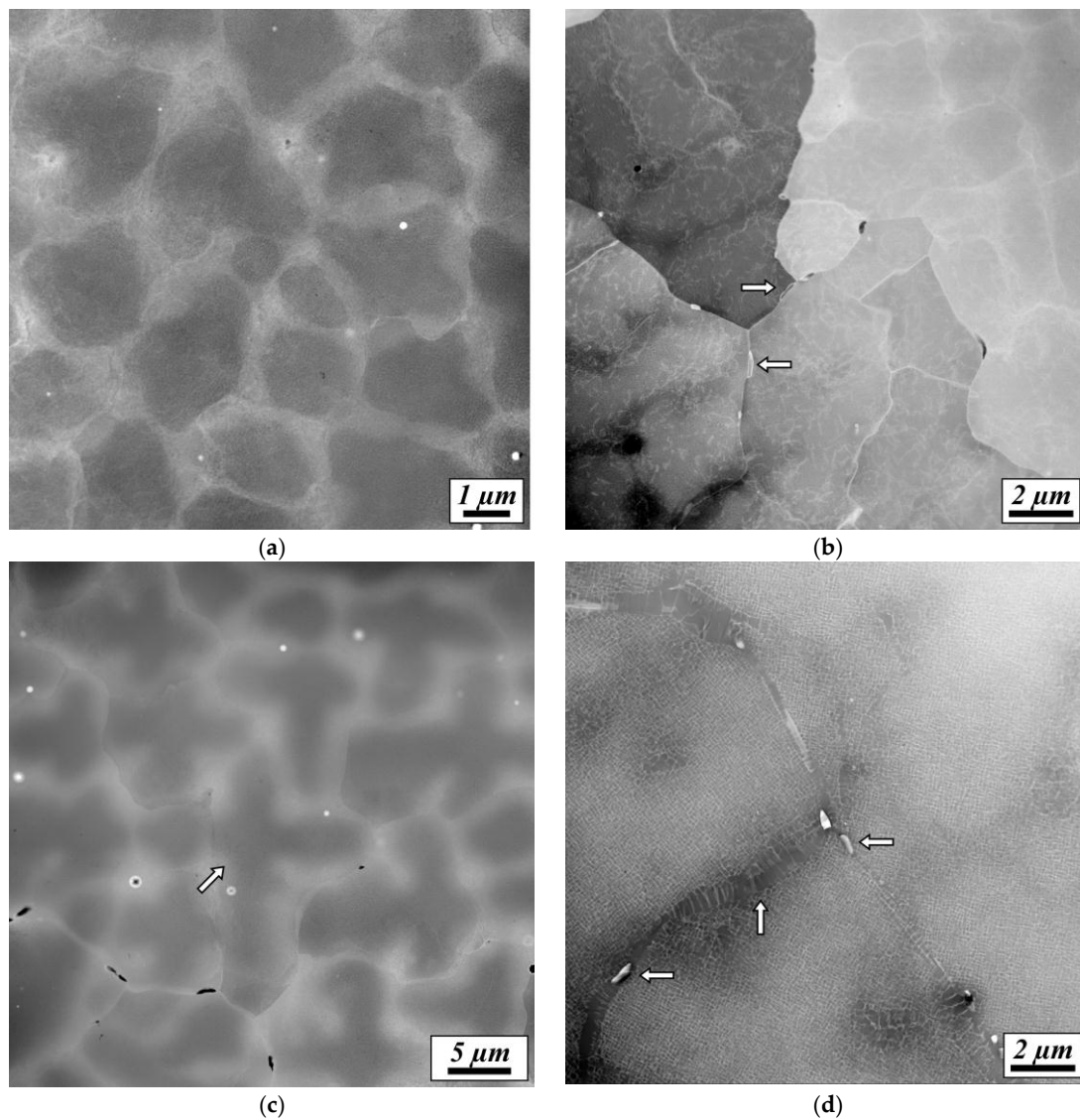


Figure 6. STEM-HAADF images showing the microstructures of materials states A and B: (a) higher magnification image of SEBM material A; (b) SEBM material A at a lower magnification; (c) low magnification image of SEBM material B; and (d) SEBM material B at a higher magnification.

Figure 7 shows a STEM micrograph of small particles highlighted by white horizontal arrows in Figure 6b,d at a higher magnification. The particles appear in a microstructural environment that mainly consist of a dark γ' phase region which extends along the boundaries. The fact that this dark region is γ' phase was proved by selected area electron diffraction (not shown here). The small brighter particles were identified as μ phase particles using selected area electron diffraction (SAD). The inset in the upper left of Figure 7 represents an indexed SAD pattern of the μ phase particle in the lower left of Figure 7. This figure suggests that the particles line up along the boundary, always in contact with the dark γ' phase.

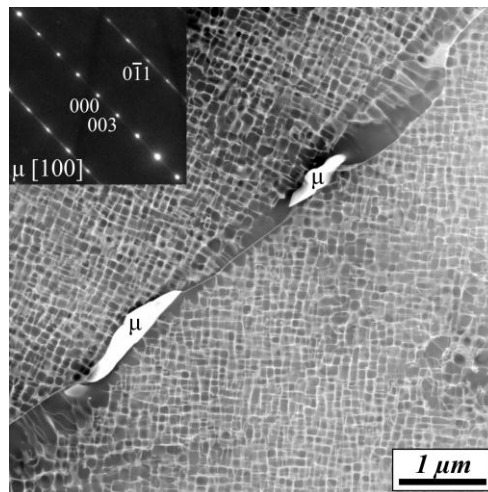


Figure 7. STEM-HAADF micrograph from SEBM Specimen B showing a dark grain boundary γ' phase and μ phase particles. The SAD pattern in the upper left, which can be indexed for μ phase, was taken from the particle in the lower left (for details see text).

In Figure 8, STEM micrographs of Specimen B are shown. Figure 8a shows a central dendrite (directions of secondary dendrite arms schematically indicated by a dashed cross) is surrounded by four interdendritic regions which show globular microstructures (highlighted by four white arrows). The region highlighted with a white vertical arrow pointing up is shown at a higher magnification in Figure 8b. The globular features of the microstructure in the center of the image can be clearly distinguished from the surrounding γ/γ' microstructure. The directions of the γ channel networks around the globular region are indicated by four fine white reference grids in Figure 8b. The four grids in Figure 8b are all parallel and show that the orientations of the γ channel networks which surrounds the globular regions are similar.

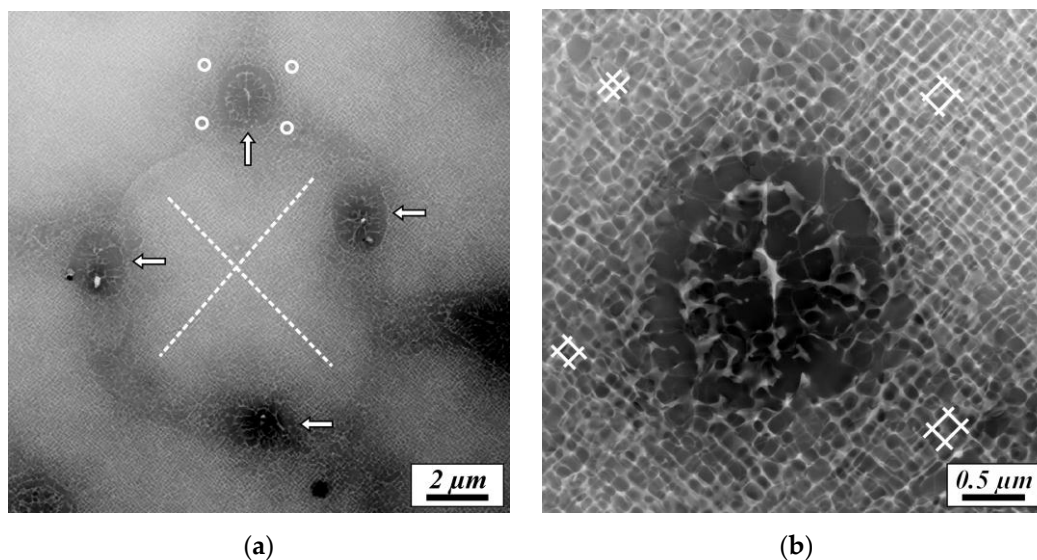


Figure 8. STEM-HAADF microstructures in Specimen B: (a) central dendrite surrounded by interdendritic regions with globular microstructures; and (b) globular region highlighted by vertical white arrow in Figure 8a at higher magnification.

So far, the presence of dendrites, interdendritic regions and μ phase particles has been discussed. Now focus is shifted on the presence of dislocations and subgrain boundaries in the microstructures of

the SEBM materials. Figure 9 shows STEM micrographs which were taken from Specimen A at a similar magnification as the image shown in Figure 6b. The image was taken in multiple beam contrast with beam direction close to [001] which allows to image the maximum number of dislocations for different microscopic crystallographic slip systems for an fcc crystal. In Figure 9, a thinner region of the TEM foil was investigated than in Figure 6 to provide much better dislocation contrast. Dislocation segments appear as small white lines in Figure 9a. The micrograph shown in Figure 9a (multiple beam diffraction contrast) shows that there is an overall high density of dislocations. The dislocations form subgrain boundaries, which are located between dendrites. However, not all adjacent dendrites are separated by subgrain boundaries. Figure 9a shows that there are ingrown nests of dislocations, several are highlighted by white arrows. These appear to be located in interdendritic regions. In the upper part of Figure 9b one ingrown nest of dislocations is shown at a higher magnification in the upper part of the image.

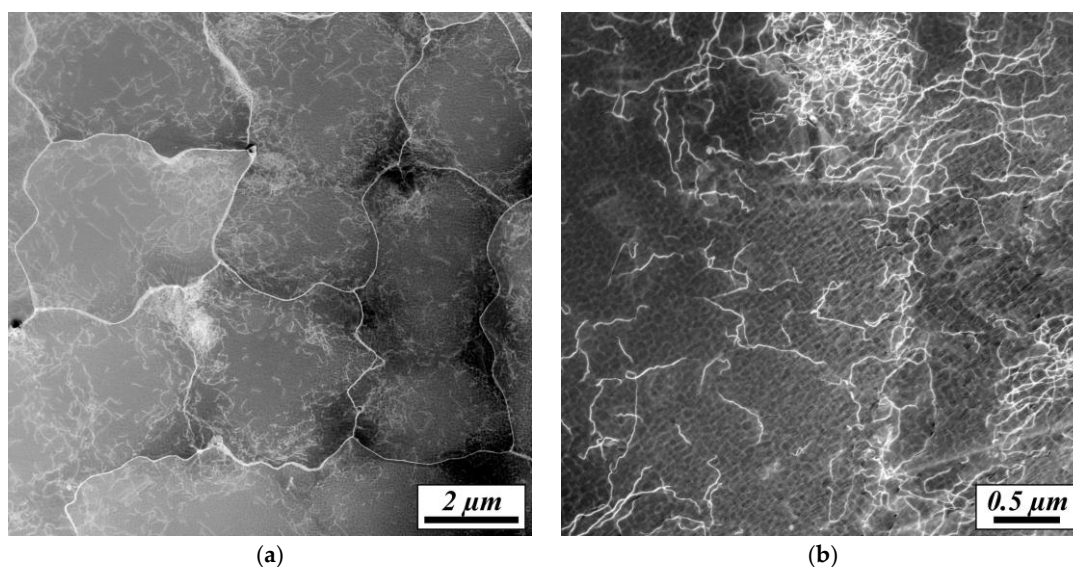


Figure 9. STEM-HAADF micrographs of the dislocation substructure in SEBM Specimen A: (a) overall high dislocation density, subgrain boundary network and ingrown nests of dislocations; and (b) ingrown dislocation nest in an interdendritic region at higher magnification.

It is interesting to look at two STEM images shown in Figure 10a,b (multiple beam contrast). Parallel to the left border of Figure 10a runs a micro grain boundary which extends over several micrometers and shows a strong bright contrast. The misorientation angle was determined as lower than 3° evaluating the Kikuchi line diffraction patterns on both sides of the boundary. Three locations along the boundary are marked with 1, 2, and 3. At these three locations, dislocations from the left side of the interface are in direct contact with the boundary. At location three, there is a distinct recess, which is shown at a higher magnification in Figure 10b. It appears as if dislocations were frozen-in while building the subgrain boundary. Figure 10a suggests that this apparent recovery process, which minimizes the overall strain energy, is completed at locations 1 and 2, while it was still ongoing at location 3.

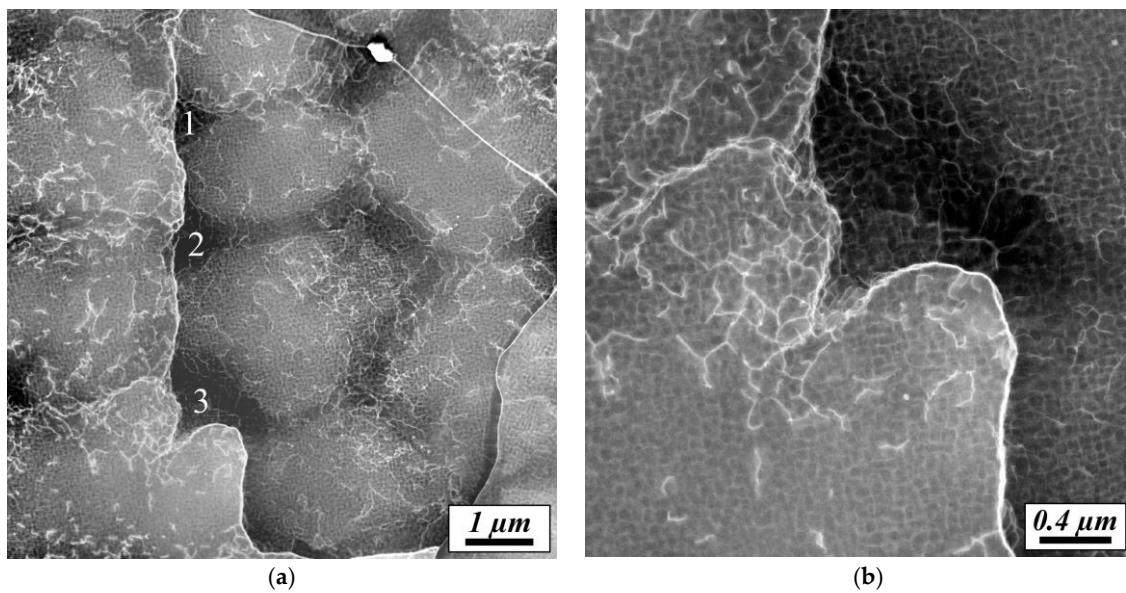


Figure 10. STEM-HAADF micrographs of the dislocation substructure in SEBM Specimen A. (a) Small angle boundary which separates two groups of dendrites. The orientation between the two regions left and right of the subgrain boundary is below 3° ; (b) The recess in the lower part of the boundary in Figure 10a at higher magnification.

In Figure 11, a microstructural region is shown with dendrites and interdendritic regions together with qualitative element distribution maps as measured using EDX. The results presented in Figure 11 suggest that the segregation tendencies in the fine scale SEBM microstructure are similar as those which are observed in conventional SX cast alloys. Especially, Co and Re show a tendency to partition to the dendrites, while Al and Ti are enriched in the interdendritic regions.

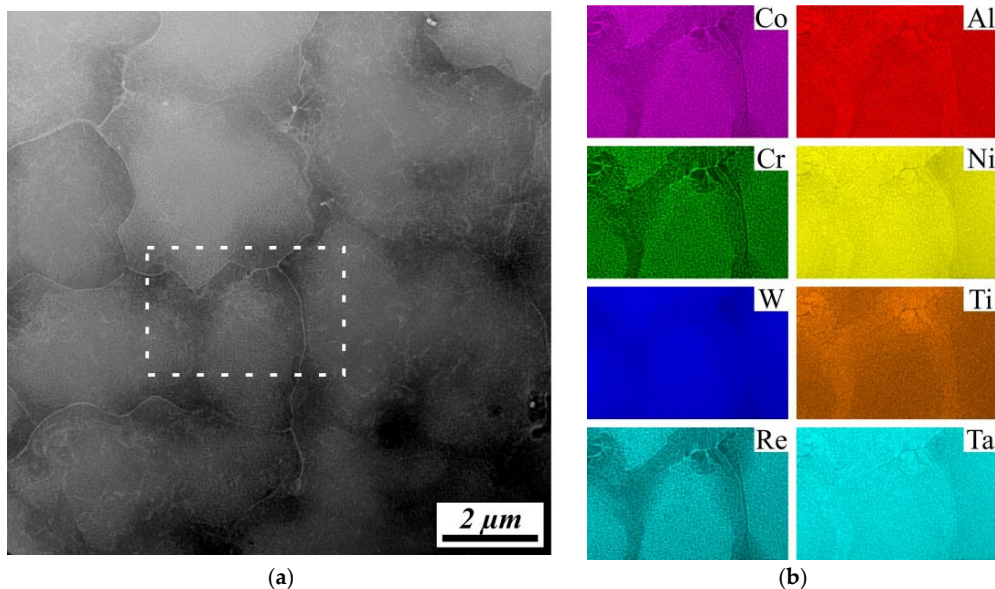


Figure 11. Element distribution in the SEBM microstructure of Specimen A. (a) STEM-HAADF image of a microstructural region which contains dendrites and interdendritic regions (2 μm scale); multiple beam condition; (b) Corresponding element distribution maps, color coded as indicated.

In Figure 12, the γ/γ' microstructure from a dendritic region of SEBM Specimen A is presented. It can be clearly seen that γ' particle sizes are in between 50 and 100 nm, Figure 12a. The small particles do not exhibit the regular cuboidal shape, which characterizes larger γ' particles in conventional SX cast alloys [5]. However, using a line intersection method, one can estimate the γ' volume fraction in Figure 12a as close to 70%. The partitioning tendencies are shown in the element distribution maps presented in Figure 12b. Similar to what was observed on the length scale of the solidification microstructure, the partitioning behavior in the γ/γ' microstructure also follows the trends which are known from conventional SX cast materials. Especially, Re partitions to the γ channels and Al is enriched in the γ' phase.

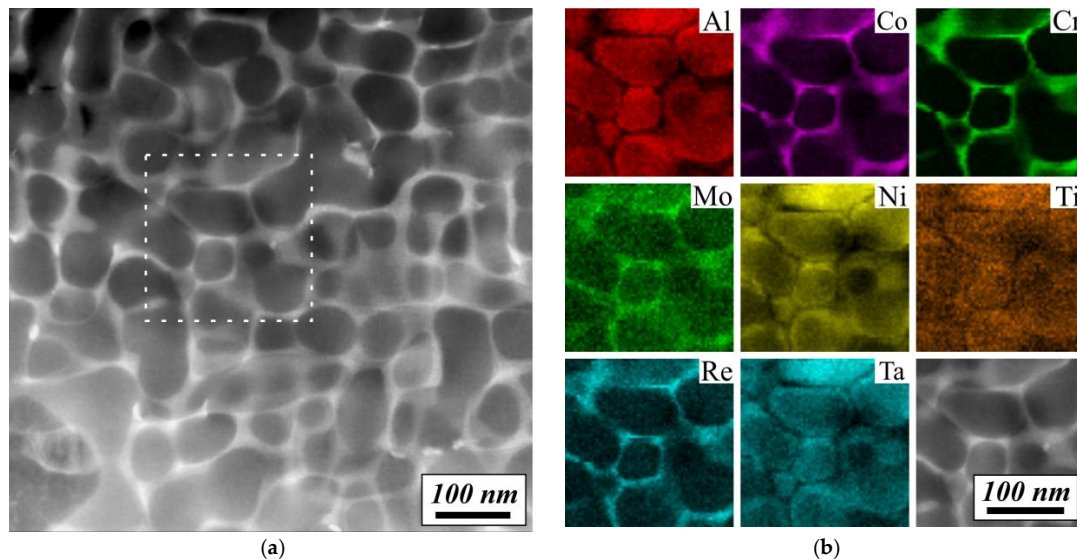


Figure 12. Distribution of alloy elements in the SEBM microstructure of Specimen A. (a) STEM-HAADF image of the γ/γ' microstructure (200 nm scale); multiple beam condition, beam close to [001] crystallographic direction; (b) Corresponding element distribution maps, color coded as indicated.

For comparison STEM micrographs of the γ/γ' microstructures in SEBM Specimens A and B are shown, Figure 13a,b. In all cases HR TEM shows that the γ' particles are coherently precipitated in the γ matrix. Figure 13 shows three TEM images. The γ' particles of Specimen A (fast cooling) in Figure 13a are significantly smaller than the γ' particles in Figure 13b, with both specimens showing a similar γ' volume fraction close to 70%. It appears that the large γ' particle size of Specimen B is associated with more pronounced cuboidal particle shape than in the case of Specimen A. Figure 13c shows a high resolution TEM (HRTEM) image of two γ' particles and the γ region in-between. The three inset FFT (fast Fourier transformation) patterns document that the three phases show the same orientation. It is also shown that the γ/γ' interfaces are not flat.

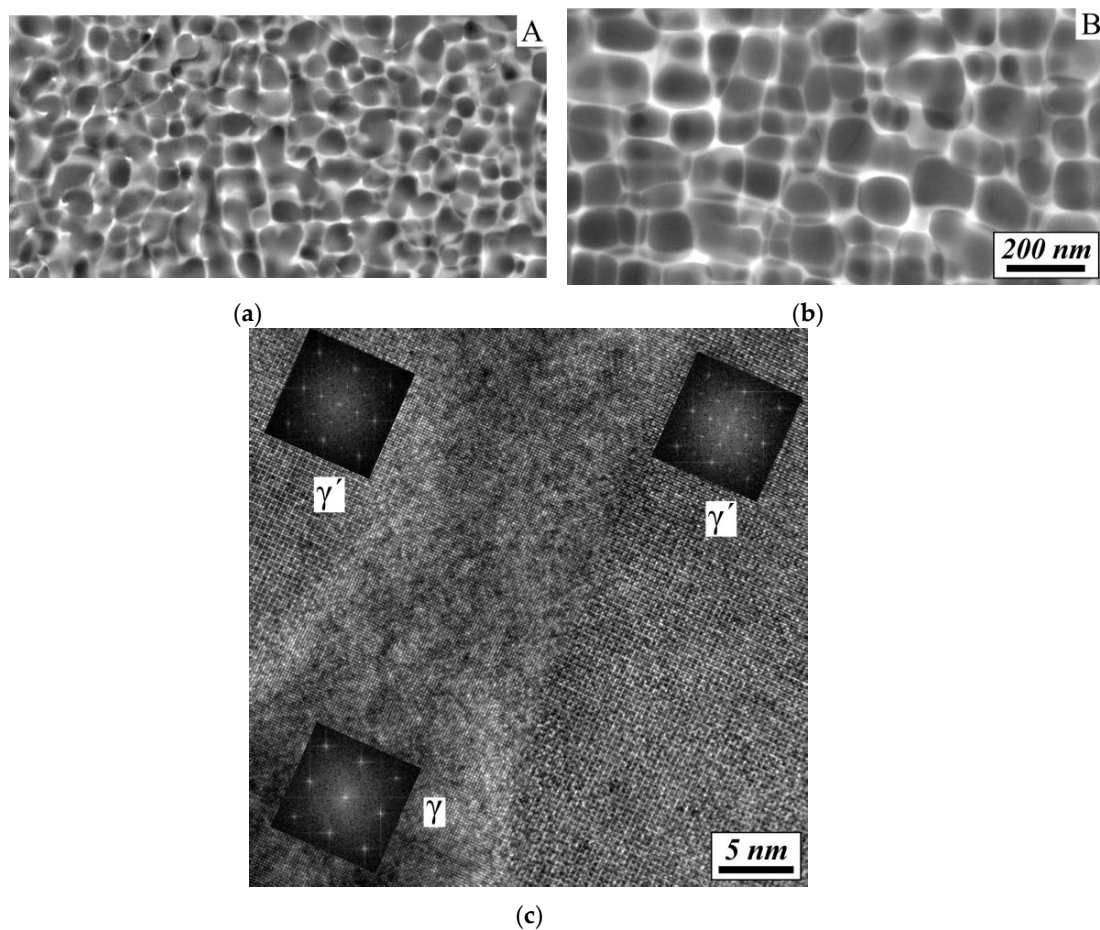


Figure 13. STEM-HAADF images documenting γ/γ' microstructures in SEBM Specimens A and B at higher magnifications: (a) smaller γ' particles in Specimen A; (b) larger γ' particles in Specimen B; and (c) HRTEM (high resolution TEM) micrograph together with calculated FFT (fast Fourier transformation) patterns showing a thin γ channel in between two coherent γ' particles.

In Figure 14, results obtained from STEM stereo analysis from grain boundaries in SEBM Specimen B are presented. Figure 14a,b shows anaglyphs which provide a 3D impression when viewed with colored glasses as indicated (left eye: red glass, right eye: cyan glass). Figure 14a shows a γ' phase grain boundary region which separates two grains. The two microstructural regions on the left and on the right of the boundary seem to be bridged by coarse γ' particles, which are separated by thin γ channels. The image suggests that the γ' volume fraction in the grain boundary region is higher than in the neighboring grains. At small angle grain boundaries this type of grain boundary microstructure is not observed (Figure 14b). Instead, one can clearly resolve low angle boundaries which are built up from dislocations. Tilt experiments allow distinguishing three types of dislocation networks in the three boundary regions. In Figure 14b one family of dislocations of a subgrain boundary network is in good contrast for the selected g vector. Further work is required to investigate the morphologies of these interesting subgrain boundary microstructures.

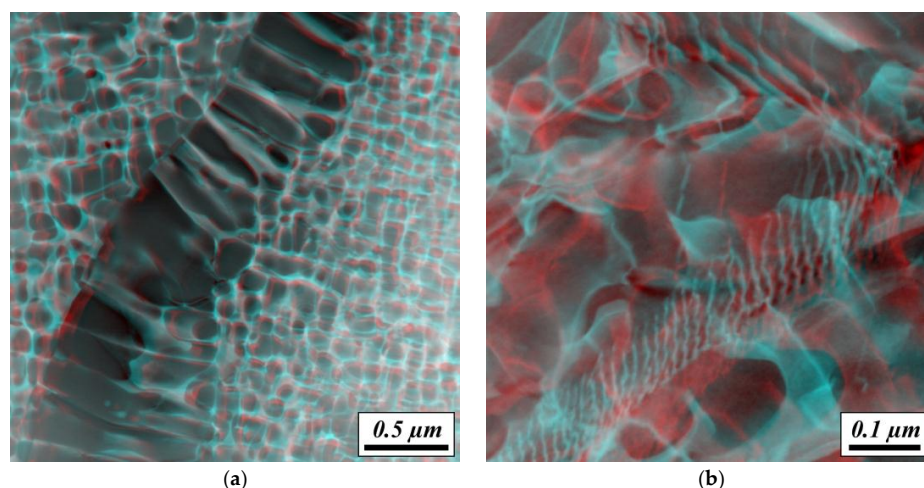



Figure 14. Anaglyphs showing grain boundary microstructures in SEBM Specimen B: (a) high angle grain boundary with coarse γ/γ' microstructure; and (b) low angle grain boundaries representing dislocation networks. For details see text. (for 3D impression use colored glasses: )

4. Discussion

The results of the present study confirm that SEBM allows creating superalloy microstructures that show many of the features which characterize conventionally cast Ni-base single crystal superalloys (e.g., [5]). One can find prior dendritic and interdendritic regions, Figures 8 and 12, and Reference [14]. These show the well-known γ/γ' microstructure (Figures 12 and 14). The γ' volume fractions are close to 70% and the partitioning of alloy elements between D and ID regions (large scale heterogeneity, Figure 11), γ channels and γ' particles (small scale heterogeneity) corresponds to what is known from conventionally cast Ni-base superalloys (e.g., [5]). They are in reasonable agreement with what are expected from thermodynamic calculations [18]. In Table 3, some average microstructural parameters of a cast Ni-base superalloy are compared with the results for the SEBM material which were produced using CMSX 4 type powder. The parameters listed in Table 3 show that while equilibrium volume fractions in SEBM and conventionally processed materials are similar, SEBM microstructures are much finer. SEBM establishes a microstructure, which is as close to equilibrium as the microstructure of a cast SX material. In the SEBM specimens, dendrite spacings are two orders of magnitude smaller than in a cast and heat treated SX materials. As can be seen from Table 3, SEBM processing also results in much smaller γ' particle sizes and γ channel widths. It is well known, that dendrite spacings depend on the cooling rate during solidification while γ' particle sizes and γ channel widths are also affected by the subsequent heat treatment (during heat treatment of SX materials, respectively, during temperature exposure during SEBM processing).

Table 3. Comparison of microstructural parameters (average values) of cast CMSX-4 single crystal and SEBM CMSX-4.

Parameter	CMSX-4 (SX)	SEBM-A	SEBM-B
γ' volume fraction	77% (ID)	77% (ID)	72% (ID)
γ' size	442 nm [19]	53 ± 17 nm	82 ± 28 nm
γ channel width	65 nm [19]	16 ± 8 nm	32 ± 23 nm
dendrite spacing	519 μ m [5]	2.1 μ m, Figure 5	7.3 μ m, Figure 5
partitioning of Al	to ID/ γ' [5]	to ID/ γ' , Figure 11	not determined
partitioning of Re	to D/ γ [5]	to D/ γ , Figure 11	not determined
dislocation density	71,012 [20]	very high, Figures 9 and 10; *	low, Figure 6 *

* Both higher than in cast alloy.

The smaller dendrite spacings in Specimen A and B as compared to the microstructure of a conventional superalloy [5] are obviously related to much higher cooling rates during SEBM processing. The goal of the present work was to explain which microstructure parameters can be observed in SEBM materials. Since there presently is no well-established SEBM procedure, two SEBM materials that are expected to have different microstructures are used. Our microstructural results allow concluding that the different SEBM process strategies used for processing Specimens A and B result in faster effective cooling rates in Specimen A, related to differences in scan strategies and of geometry/TEM specimen locations. Further work is required to systematically study how microstructure change with specific SEBM parameters. The temperature time history, which the materials experience during SEBM processing, depends on a number of parameters. One important parameter to be considered is the build temperature, T_B , which was 1150 K in both cases. Two other key parameters are the beam energy and the scanning speed, Table 3. The ratio of these two parameters yields line energies of as 0.2 J/mm and 0.6 J/mm for Specimens A and B, respectively. The higher energy input in Specimen B partly rationalizes lower effective cooling rates. Another factor is the smaller size of Specimen B. Moreover, both scanning procedures described in Figure 1b are associated with re-melting processes, which differ in nature when comparing the SEBM strategies of Specimens A and B. Last but not least, it matters where the TEM foil was taken from the SEBM specimen. Figure 2c,d show that the TEM foil from Specimen A was taken from a near surface region where cooling is faster than in the center of the specimen. In contrast, the TEM foil for Specimen B stems from the center of the specimen. This qualitative assessment allows concluding that SEBM Specimen B experienced a lower effective solidification rate than Specimen A, and therefore shows a coarser solidification microstructure. However, it is by no means easy to provide a quantitative description of the time temperature history in all locations of the SEBM specimens.

The larger γ' particle sizes and γ channel widths in our reference cast SX (Table 3, [19]) are simply related to a more intense temperature exposure during the post cast solution/precipitation heat treatment of the SX alloy. It has been shown that similar γ' particle sizes and γ channel widths can be obtained in SEBM materials by appropriate solution/precipitation heat treatments which follow SEBM processing [4].

One striking feature of SEBM Specimen A is its high dislocation density, Figures 5 and 6. From a fundamental point of view, this opens new possibility to shed some light onto two areas which are difficult to investigate in conventionally cast SX. First, in conventionally cast SX, one cannot easily locate ingrown nests of dislocations. Dislocations can only be analyzed in the TEM, where a typical width of a thin foil region is 20 μm , while spacings between interdendritic regions where dislocation nests are located [21] are much larger. In contrast, TEM specimens taken from SEBM materials allow producing foils, where one can find several ingrown nests of dislocations in one micrograph (Figure 9). Second, TEM investigations of SEBM specimen can help to study the elementary dislocation processes which govern the formation of small angle grain boundaries, Figure 10. Further work is required to exploit these possibilities. From a technological point of view, this high dislocation density may well raise concerns, because it reflects the presence of high internal stresses, which can give rise to the formation of cracks as has been discussed in the literature [14].

5. Summary and Conclusions

In the present work, advanced scanning and transmission electron microscopy is used to study the microstructures of two specimens, which were prepared by selective electron beam melting (SEBM) using a CMSX-4 powder. From the results obtained in the present work the following conclusions can be drawn:

- (1) Two microstructural results suggest that Ni-base superalloys produced by SEBM have microstructures close to thermodynamic equilibrium. Their γ' volume fractions are similar to those which are observed after conventional SX casting and post-cast heat treatment.

The partitioning behavior of alloy elements to dendritic/interdendritic regions (large scale heterogeneity) and to γ' particles/ γ channels (small scale heterogeneity) is similar.

- (2) The as-built SEBM microstructure shows all features that characterize the conventional solidification microstructures (dendrites, interdendritic regions, etc.). However, dendrite spacings are two orders of magnitude smaller than observed after SX casting. The smaller scale is beneficial, because it shortens the diffusion distances, which are required for homogenization during solution heat treatments.
- (3) The as-built SEBM microstructures feature elongated grains, which grow into the build direction of the SEBM process. All grains show close to $\langle 100 \rangle$ growth directions. EBSD results show that the columnar grains can be separated by low and high angle grain boundaries. On high angle grain boundaries, one finds coarse γ/γ' microstructures (frequently) and TCP phase particles (μ phase type, occasionally). High angle grain boundaries result from rotations around the $\langle 100 \rangle$ build direction.
- (4) The results obtained in the present study show that SEBM microstructures strongly depend on a number of parameters, which all combine to yield an effective cooling rate. SEBM specimens that experience higher effective cooling rates show finer solidification microstructures, i.e., smaller dendrite spacings. Effective cooling rates are governed by the SEBM line energy, the scan strategy and the build temperature.
- (5) A striking feature of as processed SEBM specimens that were subjected to high cooling rates is a high dislocation density. From a fundamental point of view, this opens new possibilities for the investigation of elementary dislocation processes in the microstructure of Ni-base superalloys. From a technological point of view, this indicates the presence of high internal stresses that may well give rise to the formation of cracks.

Acknowledgments: The authors acknowledge funding by the Deutsche Forschungsgemeinschaft (DFG) through projects A2 (ABP, GE, CS, and AK) and B2 (MR, and CK) of the Collaborative Research Center SFB/TR 103 on superalloy single crystals.

Author Contributions: A.B.P. and C.S. performed the TEM investigation. M.R. and C.K. manufactured the SEBM samples. A.K. carried out the EBSD study. A.B.P. and G.E. interpreted the data and wrote the paper.

Conflicts of Interest: The authors declare no conflict of interest.

References

1. Reed, R.C. *The Superalloys: Fundamentals and Applications*; Cambridge University Press: Cambridge, UK, 2008.
2. Bürgel, R.; Maier, H.-J.; Niendorf, T. *Handbuch Hochtemperatur-Werkstofftechnik: Grundlagen, Werkstoffbeanspruchungen, Hochtemperaturlegierungen und -beschichtungen*; Vieweg+Teubner Verlag: Wiesbaden, Germany, 2011.
3. Durand-Charre, M. *The Microstructure of Superalloys*; Taylor & Francis: Amsterdam, The Netherlands, 1998.
4. Ramsperger, M.; Roncery, L.M.; Lopez-Galilea, I.; Singer, R.F.; Theisen, W.; Körner, C. Solution Heat Treatment of the Single Crystal Nickel-Base Superalloy CMSX-4 Fabricated by Selective Electron Beam Melting. *Adv. Eng. Mater.* **2015**, *17*, 1486–1493. [[CrossRef](#)]
5. Parsa, A.B.; Wollgramm, P.; Buck, H.; Somsen, C.; Kostka, A.; Povstugar, I.; Choi, P.-P.; Raabe, D.; Dlouhy, A.; Müller, J.; et al. Advanced scale bridging microstructure analysis of single crystal Ni-Base superalloys. *Adv. Eng. Mater.* **2015**, *17*, 216–230. [[CrossRef](#)]
6. Mälzer, G.; Hayes, R.W.; Mack, T.; Eggeler, G. Miniature specimen assessment of creep of the single-crystal superalloy LEK 94 in the 1000 °C temperature range. *Metall. Mater. Trans. A.* **2007**, *38*, 314–327. [[CrossRef](#)]
7. Buck, H.; Wollgramm, P.; Parsa, A.B.; Eggeler, G. A quantitative metallographic assessment of the evolution of porosity during processing and creep in single crystal Ni-base super alloys. *Mater. Werkst.* **2015**, *46*, 577–590. [[CrossRef](#)]
8. Eggeler, G. *Assessment of High Temperature Fatigue Activities in the European Research Project COST 50 (Rounds I-III)*; Marriott, J.B., Ed.; Commission of the European Communities, Institute of Advanced Materials, Joint Research Centre: Petten, The Netherlands, 1992.

9. Giamei, A.F.; Tschinkel, J.G. Liquid metal cooling: A new solidification technique. *Met. Trans. A* **1976**, *7*, 1427–1434. [[CrossRef](#)]
10. Ackelid, U.; Svensson, M. Additive Manufacturing of Dense Metal Parts by Electron Beam Melting. In Proceedings of the Materials Science and Technology Conference, Pittsburgh, PA, USA, 25–29 October 2009.
11. Heinel, P.; Körner, C.; Singer, R.F. Selective electron beam melting of cellular titanium: Mechanical properties. *Adv. Eng. Mater.* **2008**, *10*, 882–888. [[CrossRef](#)]
12. Murr, L.E.; Martinez, E.; Gaytan, S.M.; Ramirez, D.A.; Machado, B.I.; Shindo, P.W.; Martinez, J.L.; Medina, F.; Wooten, J.; Ciscel, D.; et al. Microstructural architecture, microstructures and mechanical properties for a Nickel-Base superalloy fabricated by electron beam melting. *Metall. Mater. Trans. A* **2011**, *42*, 3491–3508. [[CrossRef](#)]
13. Helmer, H.E.; Körner, C.; Singer, R.F. Additive manufacturing of nickel-based superalloy Inconel 718 by selective electron beam melting: Processing window and microstructure. *J. Mater. Res.* **2014**, *29*, 1987–1996. [[CrossRef](#)]
14. Ramsperger, M.; Singer, R.; Körner, C. Microstructure of the Nickel-Base superalloy CMSX-4 fabricated by selective electron beam melting. *Metall. Mater. Trans. A* **2016**, *47*, 1469–1480. [[CrossRef](#)]
15. Jácome, L.A.; Eggeler, G.; Dlouhý, A. Advanced scanning transmission stereo electron microscopy of structural and functional engineering materials. *Ultramicroscopy* **2012**, *122*, 48–59. [[CrossRef](#)] [[PubMed](#)]
16. Schwartz, A.J.; Kumar, M.; Adams, B.L. *Electron Backscatter Diffraction in Materials Science*; Kluwer Academic Publishers: New York, NY, USA, 2000.
17. Randle, V.; Engler, O. *Introduction to Texture Analysis*; CRC Press: London, UK, 2000.
18. Yardley, A.; Povstugar, I.; Choi, P.-P.; Raabe, D.; Parsa, A.B.; Kostka, A.; Somsen, C.; Dlouhy, A.; Neuking, K.; George, E.P.; et al. On local phase equilibria and the appearance of nanoparticles in the microstructure of single crystal Ni-base superalloys. *Adv. Eng. Mater.* **2016**. [[CrossRef](#)]
19. Wu, X.; Wollgramm, P.; Somsen, C.; Dlouhy, A.; Kostka, A.; Eggeler, G. Double Minimum Creep of Single Crystal Ni-base Superalloys. *Acta Mater.* **2016**, *112*, 242–260. [[CrossRef](#)]
20. Parsa, A.B. The Role of Dislocations in the Microstructural Evolution during Creep of Single Crystal Superalloys with γ/γ' Microstructure. Ph.D. Thesis, Ruhr-Universität-Bochum, Shaker Verlag, Aachen, Germany, 2016.
21. Pollock, T.; Argon, A. Creep resistance of CMSX-3 nickel base superalloy single crystal. *Acta Metall. Mater.* **1992**, *40*, 1–30. [[CrossRef](#)]



© 2016 by the authors; licensee MDPI, Basel, Switzerland. This article is an open access article distributed under the terms and conditions of the Creative Commons Attribution (CC-BY) license (<http://creativecommons.org/licenses/by/4.0/>).